Cladding-modulated Bragg gratings in silicon waveguides

D. T. H. Tan,* K. Ikeda, and Y. Fainman

Department of Electrical and Computer Engineering, University of California San Diego, 9500 Gilman Drive, La Jolla, California 92093-0409, USA

**Corresponding author: thtan@ucsd.edu*

Received January 16, 2009; revised March 19, 2009; accepted March 24, 2009; posted March 26, 2009 (Doc. ID 106440); published April 22, 2009

A cladding-modulated Bragg grating implemented using periodic placements of cylinders along a waveguide is proposed in a silicon-on-insulator platform. The coupling strength is varied by changing the distance between the cylinders and the waveguide. This implementation enables precise control and a wide dynamic range of coupling strengths and bandwidths that can be practically achieved for applications with specific bandwidth requirements. Modeling results are verified experimentally, and we demonstrate coupling strengths differing by 1 order of magnitude (43 and 921 per cm) with bandwidths of 8 and 16 nm, respectively. This method scheme enables weakly coupled devices with high fabrication tolerance to be realized.

OCIS codes: 130.2790, 130.7408, 130.3120.

Bragg gratings are a fundamental component in optical devices, such as switching, wavelength division multiplexing (WDM), and sensing [1,2]. Recently, significant research effort has gone into realizing resonant structures in a silicon-on-insulator (SOI) material platform owing to its compatibility with standard microelectronics fabrication processes and its potential ability to realize chip-scale integrated compact optical devices. These efforts aim to exploit the miniaturization of optical circuits made possible by the high index contrast between silicon and its oxide. As a result of the high index contrast, modes under the Bragg conditions in silicon waveguides are often strongly coupled. Previously, sidewall-modulated distributed resonant structures (S-DRS) using a single-step lithography process were demonstrated [3–6]. The S-DRS offered the benefits of simpler fabrication using single-step lithography over surface relief gratings [7]. However, a drawback of the S-DRS is that the strength of the coupling coefficient is determined by the amplitude of the modulation, which in turn is limited by the resolution of electron beams used to pattern these structures. Therefore, the dynamic range and resolution of the modulation depth and consequently that of the coupling coefficient of the S-DRS are limited. Certain devices, such as narrow-bandwidth WDM components, require Bragg gratings to have weak and precisely controlled coupling coefficients. In this Letter, we introduce a cladding-modulated distributed resonant structure (C-DRS) implemented in SOI that overcomes the current S-DRS limitations in the dynamic range, resolution, and precise control of the coupling strength. To the best of our knowledge, this is the first demonstration of the proposed concept. The coupling under the Bragg matching condition is implemented using periodic placements of silicon cylinders in the cladding at a fixed distance from a single-mode silicon waveguide. The coupling strength of the C-DRS depends on the diameter and the distance of the periodically placed silicon cylinders allowing small values of coupling strength necessary to achieve narrow spectral response characteristics to be achieved. We present the design and numerical simulations of example devices as well as their fabrication and experimental validation.

The C-DRS device is shown schematically in Fig. 1 and consists of a central single-mode silicon waveguide and a periodic array of silicon cylinders of diameter W, situated a distance d from the edge of the waveguide, and with period Λ_B. W is chosen to be 200 nm to avoid supporting resonant modes inside the cylinders. The period of the cladding modulation Λ_B will be chosen to satisfy the Bragg condition at a wavelength of about 1.55 μm for the TE-polarized mode. The waveguide cross section is chosen to be single mode at 1.55 μm as indicated in Fig. 1. Since the field amplitude of the propagating mode decays exponentially outside the waveguide boundaries, the extent of the evanescent tails residing in the silicon cylinders and hence the strength of mode coupling can be varied by adjusting the distance d. We first calculate the coupling coefficient of the C-DRS as a function of distance, d. The coupling coefficient κ of a Bragg grating may be found using coupled-mode theory (CMT) [1,8,9],

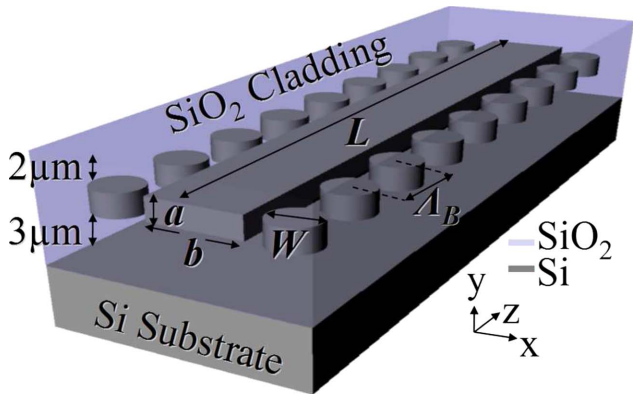

Fig. 1. (Color online) Schematic of C-DRS. Waveguide height a and width b are 250 and 500 nm, respectively. Buried oxide layer thickness=3 μm. SiO_2 overcladding thickness=2 μm.

$$\kappa = \frac{k_o}{2n_{\text{eff}}} \frac{\int_{-\infty}^{\infty}\int_{-\infty}^{\infty} \Delta n^2 \times E^2 \mathrm{d}x\mathrm{d}y}{\int_{-\infty}^{\infty}\int_{-\infty}^{\infty} E^2 \mathrm{d}x\mathrm{d}y}, \quad (1)$$

where k_o is the free-space propagation constant, Δn^2 is the refractive index perturbation, and E is the unperturbed TE-polarized electric field. A fully vectorial beam-propagation method is used to calculate the spatial distribution of the E field and the effective refractive index n_{eff} (found to be 2.63). It should be noted that for very small values of d, the CMT assumptions break down [8], and consequently, the results obtained from using CMT become less accurate; κ is found to be a function of d from Eq. (1) using the corresponding spatial distribution of the E field, and the result is shown in Fig. 2. The inverse logarithmic relationship between κ and d is a direct result of the exponential nature of the decay in modal amplitude away from the core-cladding interface.

From CMT we expect that the stop band of the device increases as the coupling strength increases. The width of the device stop band is defined here as the width between the zeros of the central lobe and may be found also from CMT [10] as

$$\Delta\lambda = \frac{\lambda^2}{n_g \times L}\left[1 + \left(\frac{\kappa \times L}{\pi}\right)^2\right]^{1/2}, \quad (2)$$

where n_g is the group index, estimated to be 3.8 [3], and L is the device length. The relationship between $\Delta\lambda$, calculated using κ found earlier, and d is plotted in Fig. 2. Two-dimensional (2D) finite-difference time-domain (FDTD) simulations conducted to confirm the device characteristics obtained from CMT are also plotted in Fig. 2. Although the numerical method includes approximations from reduction to 2D using the effective index method, it should give more accurate results than that obtained with CMT, especially for small values of d, where CMT assumptions are no longer valid. The filled and the unfilled

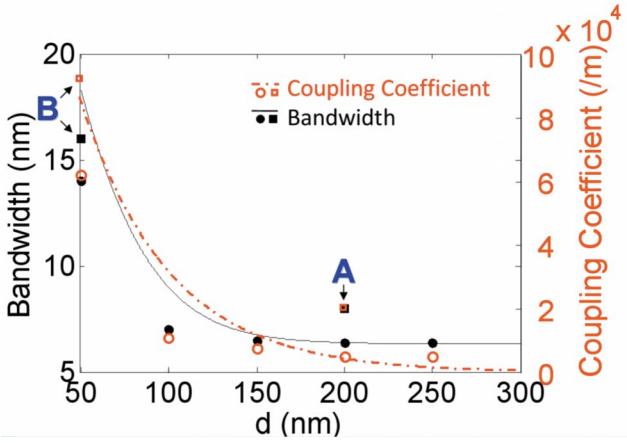

Fig. 2. (Color online) $\Delta\lambda$ (red online) and κ (black) for $W = 200$ nm and $L = 100$ μm as a function of d calculated using CMT (solid curve) and FDTD (circles). Experimental $\Delta\lambda$ and κ for devices A and B are marked with squares.

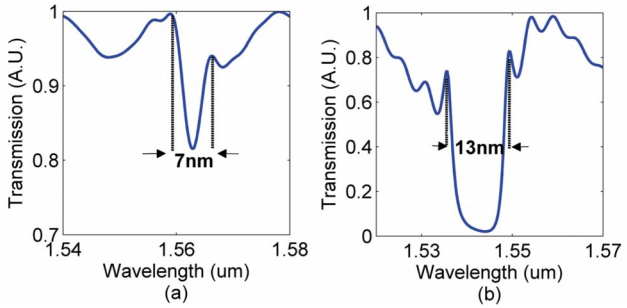

Fig. 3. (Color online) 2D FDTD simulation results. Transmission for (a) $L = 100$ μm, $d = 200$ nm, $W = 200$ nm, $\Lambda_B = 300$ nm (device A) and (b) for $L = 70$ μm, $d = 50$ nm, $W = 200$ nm, $\Lambda_B = 295$ nm (device B).

circles in Fig. 2 show the values of $\Delta\lambda$ for several devices with $L = 100$ μm found using FDTD and κ calculated from them using Eq. (2), respectively. It is evident that the disparity between $\Delta\lambda$ calculated using CMT and 2D FDTD becomes larger for small values of d owing to the decreased accuracy of CMT. We also observe in both the CMT and the FDTD plots that $\Delta\lambda$ approaches a limit of ~5 nm as d increases. For $\kappa L \ll \pi$, $\Delta\lambda$ becomes increasingly dependent on L, explaining the limiting behavior for weak coupling. For $\kappa L \gg \pi$, κ becomes the dominant factor on the value of $\Delta\lambda$.

For experimental validation, we choose two example device geometries, i.e., device A with $L = 100$ μm, $d = 200$ nm, $\Lambda_B = 300$ nm and device B with $L = 70$ μm, $d = 50$ nm, $\Lambda_B = 295$ nm. The calculated coupling coefficients, 43 and 921 cm for devices A and B, respectively, are more than 1 order of magnitude different and correspond to operation in the weak-coupling and strong-coupling regimes, respectively. Figure 3 shows the result of the transmission spectra for these two devices obtained using FDTD; $\Delta\lambda$ for the weakly coupled device is 7 nm [Fig. 3(a)], as opposed to 13 nm [Fig. 3(b)] for the strongly coupled device. Apodization to eliminate the observed sidelobes may be implemented in two ways. The first is to gradually decrease W toward the ends of the device, while the second approach involves gradually increasing the distance d toward the ends of the device. Further research on these issues is currently under investigation and will be reported in the future.

The devices with configurations A and B were fabricated on an SOI wafer with a 250 nm silicon layer and a 3 μm buried oxide layer on a silicon substrate. e-beam lithography and reactive ion etching were used to pattern and define the device geometry. An SiO_2 overcladding layer was deposited on the etched structure using plasma enhanced chemical vapor deposition. The ends of the access waveguides were terminated with inverse tapers for efficient fiber-to-waveguide coupling [11]. In particular, for device A, which possesses a small extinction ratio, the inverse tapers are necessary to prevent Fabry–Perot oscillations from washing out the transmission spectrum. Figure 4 shows scanning electron microscopes (SEM) micrographs of fabricated device B before SiO_2 deposition. The transmission spectra of the devices was

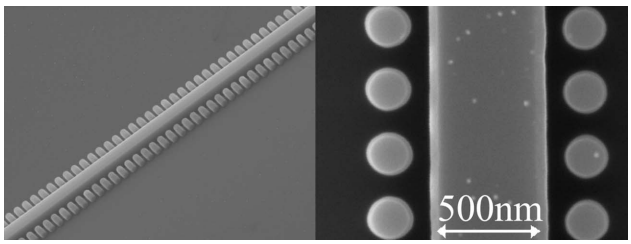

Fig. 4. SEM micrographs of fabricated devices.

measured, and the experimental results are shown in Fig. 5; $\Delta\lambda$ and the value of κ calculated using Eq. (2) for the two devices are denoted by the filled and unfilled squares, respectively, in Fig. 2. Even though $L=70\ \mu$m for device B, $\kappa L \gg \pi$ and therefore κ is the dominant factor on $\Delta\lambda$; κ calculated from Eq. (2) should therefore be similar to that for $L=100\ \mu$m. The extinction $\Delta\lambda$ and κ calculated for device B [Fig. 5(b)] show good agreement with the FDTD results presented in Fig. 3(b). The slight redshift in the position of the stop band may be attributed to the central waveguide being measured to be slightly larger than 500 nm owing to the proximity effect during the e-beam writing process, resulting in a higher n_{eff}; $\Delta\lambda$ is slightly larger than expected for both devices A {8 nm measured [Fig. 5(a)] compared with 7 nm expected [Fig. 3(a)] and B [16 nm measured (Fig. 5(b))] compared with 13 nm expected [Fig. 3(b)]}. In the case of device A, the small difference of 1 nm is well within experimental error, and the larger extinction observed is likely due to d being slightly smaller than 200 nm as a result of the larger central waveguide width. In the case of device B, the discrepancy is likely due to the cladding columns being larger than 200 nm in diameter and the distance d being smaller than that of the target value again due to the proximity effect of the e-beam writing process. The exponential relationship between d and κ implies that small deviations from the desired value of d lead to large deviations in the grating response for small values of d and less so for large values of d.

It should be noted that the demonstrated C-DRS device may be useful for on-chip switching and add–drop filtering applications. By integrating several C-DRS with slightly different values of Λ_B, the device could be used to route data at different carrier frequencies (i.e., wavelengths). For example, smaller values of κ with sufficiently long L to achieve an $\sim$100% efficiency/extinction ratio will allow a larger number of narrowband dense WDM channels, whereas a large value of κ will accommodate a fewer number of channels but each with a much wider bandwidth. To circumvent the limiting behavior of the bandwidth observed in Fig. 2, devices with small values of κ can be made longer such that $\kappa L \gg \pi$. For example, for $d=200$ nm and $L=2.3$ mm such that $\kappa L=10$, we can achieve a narrow bandwidth filter with $\Delta\lambda=0.9$ nm [see Eq. (2)].

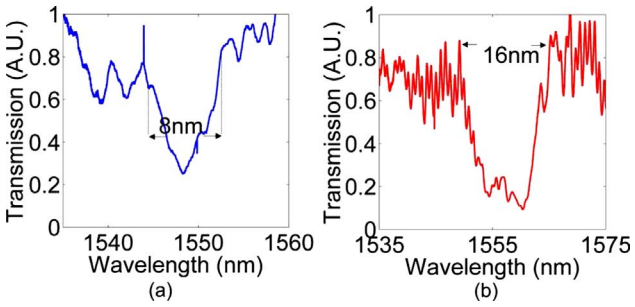

Fig. 5. (Color online) Measured transmission for (a) device A and (b) device B.

In summary, we have designed, fabricated, and experimentally validated a cladding-modulated Bragg grating using an SOI material platform that allows a large dynamic range, resolution, and precise control of the coupling strengths of the C-DRS. Devices with weak and strong coupling strengths differing by an order of magnitude were demonstrated experimentally confirming the numeric predictions. The C-DRS approach is more realistic from a fabrication standpoint compared to other on-chip Bragg grating designs, since accurate control of the separation distance d is more easily realized. This method of creating Bragg gratings enables weak-coupling coefficients to be realized to meet narrow bandwidth requirements in switching and add–drop filtering applications.

This work was supported by the Defense Advanced Research Projects Agency (DARPA), the National Science Foundation (NSF), the NSF Center for Integrated Access Networks Engineering Research Center, the United States Air Force Office of Scientific Research (AFOSR) and the United States Army Research Office (ARO). The authors acknowledge helpful suggestions from H.-C. Kim.

References

1. R. Kashyap, *Fiber Bragg Gratings* (Academic, 1999).
2. A. D. Kersey, M. A. Davis, H. J. Patrick, M. LeBlanc, L. P. Koo, C. G. Askins, M. A. Putnam, and E. J. Friebele, J. Lightwave Technol. **15**, 1442 (1997).
3. H. C. Kim, K. Ikeda, and Y. Fainman, Opt. Lett. **32**, 539 (2007).
4. K. Ikeda, M. Nezhad, and Y. Fainman, Appl. Phys. Lett. **92**, 201111 (2008).
5. D. T. H. Tan, K. Ikeda, R. E. Saperstein, B. Slutsky, and Y. Fainman, Opt. Lett. **33**, 3013 (2008).
6. J. T. Hastings, M. H. Lim, J. G. Goodberlet, and H. I. Smith, J. Vac. Sci. Technol. B **20**, 2753 (2002).
7. T. E. Murphy, J. T. Hastings, and H. I. Smith, J. Lightwave Technol. **19**, 1938 (2001).
8. A. Yariv, IEEE J. Quantum Electron. **9**, 919 (1973).
9. W. Streifer, D. R. Scifres, and R. D. Burnham IEEE J. Quantum Electron. **QE-11**, 867 (1975).
10. D. C. Flanders, H. Kogelnik, R. V. Schmidt, and C. V. Shank, Appl. Phys. Lett. **24**, 194 (1974).
11. V. R. Almeida, R. R. Panepucci, and M. Lipson, Opt. Lett. **28**, 1302 (2003).